CCS Chemistry

RESEARCH ARTICLE

Received: Aug. 4, 2022 | Accepted: Dec. 13, 2022 | Published: Jan. 4, 2023

Selective Generation of Electroreduction C_1–C_2 Products Through Self-Regulation of Catalytically Active Cu Sites on the Same Coordination Cluster Catalyst

Rui Wang[1], Jiang Liu[1,2]*, Long-Zhang Dong[1], Jie Zhou[2], Qing Huang[2], Yi-Rong Wang[1], Jing-Wen Shi[1] & Ya-Qian Lan[1,2]*

[1]*School of Chemistry and Materials Science, Nanjing Normal University, Nanjing 210023,* [2]*School of Chemistry, South China Normal University, Guangzhou 510006*

**Corresponding authors: liuj0828@m.scnu.edu.cn; yqlan@m.scnu.edu.cn; yqlan@njnu.edu.cn*

Cite this: *CCS Chem.* **2023**, Just Published. DOI: 10.31635/ccschem.022.202202316

Well-defined crystalline coordination compound catalysts have showcased distinct advantages in the regulation of the species and selectivity of electrocatalytic CO_2 reduction products. However, the systematic study of the crystal-facet effect of crystalline coordination compounds on the performance of electrocatalytic CO_2 reduction has not yet been reported. Herein, a stable hexanuclear copper cluster (Cu_6) catalyst model system is designed and synthesized. By effectively regulating the growth size (micro-nano size) and morphology of the Cu_6 single crystal, Cu_6(P) with the main (100) facet, Cu_6(H) with the main (100) and (001) facets, and Cu_6(S) with the main (001) facet are obtained. From Cu_6(P) via Cu_6(H) to Cu_6(S), there is a shift from the predominantly exposed (100) facet (involving two non-adjacent active Cu sites) to the (001) facet (involving three adjacent active Cu sites), which directly affects the adsorption direction of the key *CO intermediate and the potential of C–C coupling, thus enabling effective regulation of the selectivity of C_1 (CO and CH_4) and C_2 (C_2H_4) reduction products. This work provides an essential molecular model system and a novel design perspective for the systematic study of the crystal-facet effect of coordination compounds on the species and selectivity of CO_2 reduction reaction products.

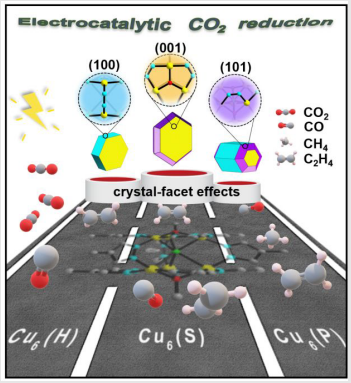

A stable hexanuclear Cu-based crystalline coordination cluster model catalyst system, a Cu_6 catalyst [Cu_6(P), Cu_6(H), and Cu_6(S)] with different naked crystal facets was demonstrated to study how the crystal facet affects the CO_2RR product.

Keywords: coordination compounds, electrocatalytic CO_2 reduction reaction, crystal-facet regulation, C–C coupling

Citation: *CCS Chem.* **2023**, Just Published. DOI: 10.31635/ccschem.022.202202316
Link to VoR: https://doi.org/10.31635/ccschem.022.202202316

Introduction

Electrocatalytic CO_2 reduction reaction (CO_2RR) is an important green conversion pathway, and the types of electrocatalysts that can realize the efficient conversion of CO_2 to specific reduction products are diverse.[1,2] Currently, high-performance catalysts for the electroreduction of CO_2 to multi-carbon products with high energy density are mainly focused on Cu-based nanomaterials,[3–5] for which a series of effective strategies, including tuning their size,[6,7] compositions,[8] crystal facets,[9–11] morphology,[12–14] oxidation states,[15,16] defects,[17] surface modification,[18,19] doping,[20] etc., are essential to investigating the electrocatalytic reaction mechanisms for the highly selective conversion of CO_2 to specific carbon-based products. Especially for the crystal-facet effect, as an important surface texture feature that directly affects the number, spatial distribution (e.g., position, distance, and angle), and the exposed coordination space for CO_2 attack, adsorption, and activation of catalytic active sites, has a great impact on the activity and selectivity of electrocatalytic CO_2 reduction products.[21–23] However, various types of catalyst structures have different catalytic mechanisms for the CO_2 reduction of specific carbon-based products.[24] Notably, some stable coordination compounds with well-defined crystal structure information as electrocatalysts not only exhibit quite excellent performance in CO_2RR, but also contribute to a deeper understanding of the catalytic reaction mechanism and the establishment of an accurate structure–activity relationship.[25] In recent years, various crystalline electrocatalysts with clear structure information have been directionally designed and synthesized by our group to realize highly selective CO_2 conversion to carbon monoxide (CO),[26] formic acid (HCOOH),[27] methane (CH_4),[28,29] ethylene (C_2H_4),[30,31] and other products. These experimental results solidly prove that they can exhibit unique advantages and equivalent performance to other catalysts in the field of electrocatalytic CO_2RR. Additionally, the number, spatial arrangement (e.g., position, distance, and angle), and the exposed coordination space for CO_2 attack of active Cu sites exposed on various facets in crystalline coordination compounds are different from those of conventional Cu-based nanomaterial catalysts.[32,33] Thus, their crystal facet regulation also has a significant impact on the formation and reaction mechanism of electrocatalytic CO_2 reduction products.

In general, most high-performance crystalline catalysts (>100 μm) are ground down to micro–nano size and then coated on a carrier as an electrode to test electrocatalytic performance.[34] In this case, the crystal facets of the crystalline coordination compound catalyst tend to be isotropic, which affects the species and selectivity of reduction products, and ultimately shows the comprehensive reduction performance of all active sites exposed by different crystal facets.[4] If their size can be reduced to the micro–nano scale and the exposed area of different crystal facets can be controlled through effective synthetic methods,[35] we can purposefully manipulate the highly active catalytic sites to be exposed as much as possible, which is very important for the improved selectivity of specific reduction products and exploring the related catalytic reaction mechanism in electrocatalytic CO_2RR.[36] Nevertheless, given the difficulties of effectively controlling the crystal growth size and crystal facets of coordination compounds, as well as the high structural stability requirements of the catalysts under the severe conditions of the electrocatalytic reaction, establishing an effective and stable coordination compounds model catalyst is the key to systematically studying the influence of the crystal-facet effect on the selectivity and reaction mechanism of carbon-based reduction products. However, such studies have not been reported to date.

Based on these considerations, we design and construct a stable model hexanuclear copper cluster, $[\{Cu_3(\mu_3\text{-}OCH_3)(\mu\text{-}MePz)_3\}_2(\mu\text{-}MePz)_3(\mu_6\text{-}Cl)]$ (denoted as Cu_6, MePz = 4-methyl-1*H*-pyrazole), which is composed of two trinuclear copper cluster $\{Cu_3\}$ units chelated by three 4-MePz ligands. It can be seen from the structure that there are obvious differences in the number and spatial arrangement of Cu active centers on different crystal facets. By the addition of alkali surfactants in situ, the growth of the crystal nucleus can be effectively controlled, and a set of Cu_6 with micro-nano crystallite size and different crystal facets exposed on the surfaces are obtained, namely, polyhedral Cu_6 (Cu_6(P)), hexagonal prism Cu_6 (Cu_6(H)), and the sheet Cu_6 (Cu_6(S)). As with nanomaterial catalysts, they can be directly coated on carbon paper maintaining the original morphology as an electrode to be applied to the electrocatalytic CO_2RR. The experimental results and the density functional theory (DFT) calculation indicate that (1) the ground Cu_6 (Cu_6(G)) (~100 nm) has a serious hydrogen evolution reduction (HER) phenomenon (~30% FE_{H2}), and the Faradaic efficiencies (FEs) of CO and C_2H_4 are 24.86% and 28.77% at −1.0 V [vs reversible hydrogen electrode (RHE)], implying that the sample after grinding cannot control the selectivity of the specific product due to the averaging of crystal facets. (2) When micro–nano crystalline morphologies of Cu_6 catalysts evolve from Cu_6(P) through Cu_6(H) to Cu_6(S), the selectivity for C_1 species (refers to CO and CH_4) gradually drops [Cu_6(P) (57.90%) > Cu_6(H) (35.58%) > Cu_6(S) (28.55%)] accordingly with the exposed area of the (100) facet (abbreviated as $S_{(100)}$). This is because the two non-adjacent Cu active sites with the long-distance and steric hindrance exposed on the (100) facets cannot effectively perform the C–C coupling, which is essentially consistent with the catalytic effect of the solitary single Cu site on the (101) facets only absorbing one *CO to generate the C_1 product. (3) At the

Citation: *CCS Chem.* **2023**, Just Published. DOI: 10.31635/ccschem.022.202202316
Link to VoR: https://doi.org/10.31635/ccschem.022.202202316

same time, the selectivity for the C_2 product (C_2H_4) gradually grows with increasing $S_{(001)}$, where the three adjacent active Cu sites with close distance on this facet are more likely to stabilize *COCO key intermediates, which is very suitable for C–C coupling to achieve the efficient conversion of CO_2 to C_2H_4. Therefore, Cu_6(S), with the largest $S_{(001)}$, shows the highest FE_{C2H4} (63.56%) with a high current density of ~390.07 mA cm^{-2} at –1.0 V. This work provides an essential Cu_6 molecular model system, and systematically investigates the influence of crystal-facet effects on the selectivity of C_1 or C_2 reduction products.

Experimental Methods

Materials

4-Methyl-1*H*-pyrazole was purchased from Shanghai Aladdin Bio-Chem Technology Corporation Ltd. (Shanghai, China). CuCl was purchased from China National Medicines Corporation Ltd. (Beijing, China). The solvents used include *N*,*N*-dimethylacetamide (DMA) and methanol (CH_3OH), which were also purchased from China National Medicines Corporation Ltd. Ammonium fluoride (NH_4F) was purchased from Shanghai Reagent (Shanghai, China). Diethylamine ($C_4H_{11}N$) was purchased from Shanghai Lingfeng Chemical Corporation Ltd. (Shanghai, China). Nafion solution (5 wt %) was purchased from Alfa Aesar Chemical Corporation Ltd. (Shanghai, China). Carbon paper was obtained from the Fuel Cell Store (Texas, United States). All chemicals and solvents were purchased and used without further purification. All solutions used in the experiments were prepared with Millipore water (18.25 MΩ). High purity gas of CO_2 (99.9995%) and Ar (99.9995%) were purchased by Nanjing Yehao.

Synthesis method of Cu_6 samples

A mixture of CuCl (0.1 mmol) and 4-methyl-1*H*-pyrazole (1 mmol) in 4 mL mixed solvent (DMA:MeOH = 1:3) was charged in a 12 mL Pyrex vial and heat at 100 °C for 4 days. After cooling at room temperature, dark-green hexagonal block crystals Cu_6 were obtained. During the synthesis process, ~8 mg of NH_4F was added, the dark-green powder Cu_6(P) was obtained. If it was replaced by 20 μL $C_4H_{11}N$, and the reaction solution was heated to 100 °C for over 72 h, a green powder Cu_6(H) was generated. Finally, the concentration of the reaction solution was doubled, and 20 μL $C_4H_{11}N$ was added in situ, and the green powder Cu_6(S) was obtained. All chemicals and solvents were purchased and used without further purification. All solutions used in the experiments were prepared with Millipore-purified water (18.25 MΩ). The detailed experimental methods and various characterization results are shown in the Supporting Information.

Preparation of gas diffusion electrodes

For Cu_6(G), 5 mg of the sample after grinding was added into 1 mL mixed solution (ethanol:water:Nafion = 6:3:1) and then sonicated for 20 min to form a mixed ink, and 50 μL of the catalyst ink was pipetted onto the center (S = 0.5 cm × 1 cm) of a carbon paper electrode (S = 1 cm × 2 cm) with a loading of 1 mg/cm^2. In the process of preparing the electrocatalyst, Nafion solution was used as an electrocatalyst dispersion liquid, which helps the catalyst evenly adhere to the surface of the carbon paper.

For Cu_6(P), Cu_6(H), and Cu_6(S), to maintain the integrity of the crystal facet in the process of preparing the catalyst, these samples do not require grinding and long-term ultrasonication and other operations are consistent with the above description.

Electrochemical measurements

All electrocatalysis testing of the catalysts were performed in an ambient environment on the electrochemical workstation (SP-150, Bio-Logic) in a three-channel flow cell configuration, including a gas-diffusion layer (GDL) as the working electrode, an anion exchange membrane (Fumasep, FAA-3-PK-130), a Pt plate as the counter electrode, and a Ag/AgCl electrode used as the reference electrode. The electrolyte (0.5 M KOH) without special treatment in the cathode and anode is circulated by a peristaltic pump (LongerPump, BT100-2J) at a flow rate of 7.4 mL min^{-1}. The high-purity CO_2 (99.9995%) gas flow rate is set as 20 sccm via a mass flow controller (AITOLY, MFC300). All the potentials are measured versus the Ag/AgCl electrode with 90% *iR* compensation, and the results are reported versus the RHE based on the Nernst equation: E (vs RHE) = E (vs Ag/AgCl) + 0.197 V + 0.059 × pH. Solution resistance (R_u) was determined by potentiostatic electrochemical impedance spectroscopy (EIS) at a sinusoidal potential frequency of 100 kHz with 20 mV amplitude centered on the electrolysis potential just before electrolysis. The potentials are converted to the RHE scale: E (iR corrected vs RHE) = E (vs RHE) – iR_u.

Reaction product analysis

The electrocatalytic CO_2RR measurements were carried out under the potential window range from –0.7 to –1.1 V (vs RHE) to obtain the reduction products. The obtained gas product was analyzed by on-line gas chromatography (GC; 7820A, Agilent) equipped with a flame ionization detector to monitor the gas products (CH_4, C_2H_4), and a thermal conductivity detector was used to analyze H_2 and CO concentrations. Four concentrations of standard mixed gases (**1**–**4**) containing H_2, CO, CH_4, C_2H_2, C_2H_4, C_2H_6, C_3H_6, and C_3H_8 with a CO_2 (mol/mol) balance were used to calculate the standard curves for GC measurements (see Supporting Information Table S1 and

Citation: *CCS Chem.* **2023**, Just Published. DOI: 10.31635/ccschem.022.202202316
Link to VoR: https://doi.org/10.31635/ccschem.022.202202316

Figure S1). The liquid products in the cathode chambers were collected during electrolysis and analyzed by nuclear magnetic resonance (NMR), in which 0.5 mL electrolyte was mixed with 0.1 mL D_2O.

Results and Discussion

Structure and characterization of Cu_6

Single-crystal X-ray diffraction (SCXRD) revealed that Cu_6 crystallizes in a hexagon with a space group of $P6_3/m$ (Supporting Information Table S2), and the asymmetric unit consists of one crystallographically independent Cu_1 atom, 1/3 μ_3-OMe, 3/2 MePz, and 1/6 μ_6-Cl (Supporting Information Figure S2). Five-coordinated Cu_1 atoms possessing a tetragonal pyramidal coordination environment were connected with three N atoms from three μ-MePz ligands on the equatorial plane, one Cl ion, and one O atom from μ_3-OMe on the axial position. As shown in Figure 1a, Cu_6 consists of two identical trinuclear units $\{Cu_3(\mu_3\text{-OMe})(\mu\text{-4-MePz})_3\}^{2+}$ (denoted as $\{Cu_3\}$; -OMe represents methoxide) bridged by three μ-4-MePz-ligands, and an encapsulated μ_6-Cl located at the center of cluster structure. The molecular structure of Cu_6 includes a C_3 symmetry axis running through one μ_6-Cl, resulting in all coordination environments of all three Cu atoms in the $\{Cu_3\}$ unit being the same (Figure 1b). Any two Cu^{2+} ions in this $\{Cu_3\}$ unit are bridged by two N atoms of one 4-MePz ligand being almost coplanar to the Cu_3 triangle covered by a μ_3-OMe group (Figure 1c). Moreover, these three Cu atoms with a close Cu–Cu distance of 3.217 Å are exactly located on the (001) facet of Cu_6 (Supporting Information Figure S3 and Figure 1d). Therefore, from the perspective of catalysis, these three identical adjacent Cu sites have sufficient coordination space to accept the attack of multiple parallel substrate molecules from the same direction. Except for the (001) facet, the number and spatial distribution of active Cu sites on other crystal facets in Cu_6 cluster also vary considerably. For example, the two non-adjacent Cu atoms with a Cu–Cu distance of 3.682 Å are positioned on the crystal facets represented by the (100) facet [abbreviated as the (100) facets] of Cu_6, which can accept the attack of multiple substrates from different directions due to spatial resistance (Figure 1e). Any

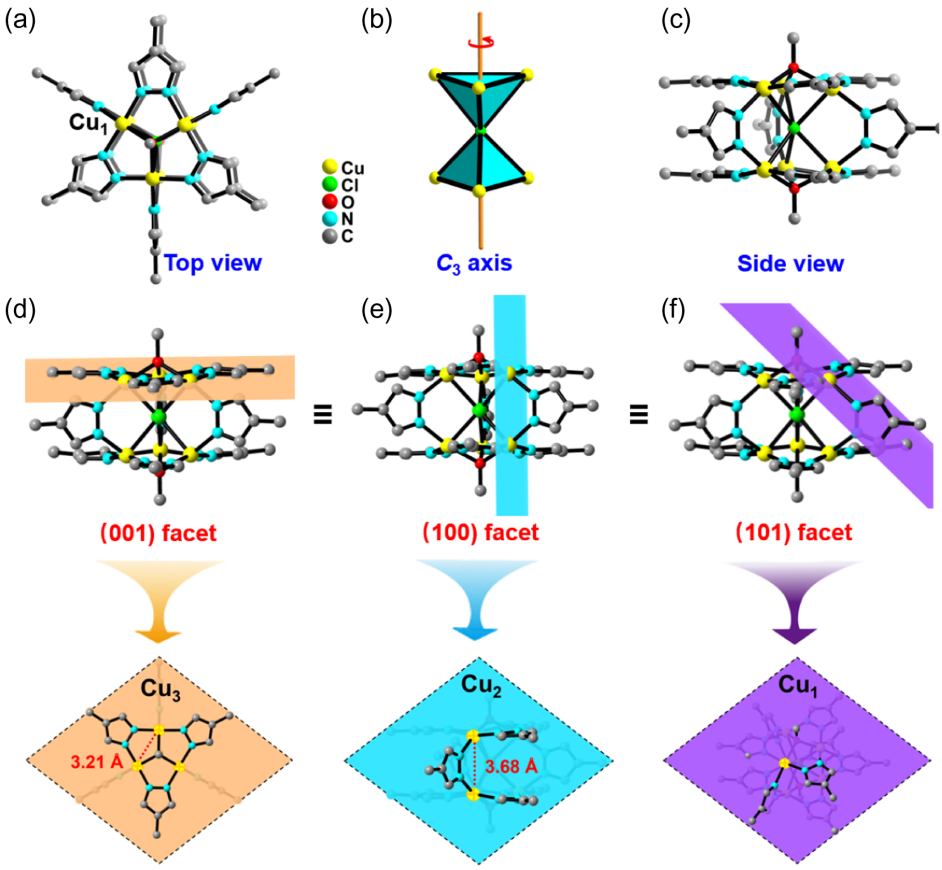

Figure 1 | *The crystal structure of Cu_6. (a) The top view. (b) The C_3 axis in Cu_6. (c) The side view. (d) The three adjacent Cu active sites marked with crosses exposed on (001) facet. (e) The two non-adjacent Cu active sites marked with crosses exposed on (100) facet. (f) The single Cu active site marked with crosses exposed on (101) facet. All hydrogen atoms are omitted for clarity.*

Citation: *CCS Chem.* **2023**, Just Published. DOI: 10.31635/ccschem.022.202202316
Link to VoR: https://doi.org/10.31635/ccschem.022.202202316

isolated Cu site located on crystal facets represented by the (101) facet [abbreviated as the (101) facets] has the same coordination environment in Cu_6 and can only accept the attack of a single substrate from different directions (Figure 1f).

The Cu_6 single crystal synthesized by the solvothermal method is a dark green regular hexagonal prism of approximately 500 μm in size, exposing the crystal facets of (001), (010), (110), and (100) determined by SCXRD (Supporting Information Figure S4). During crystal synthesis, the in situ addition of alkali surfactants can accelerate the efficiency of ligand deprotonation, which affects the growth rate of the crystal nucleus.[37] And finally, three kinds of morphologies of micro–nano-sized Cu_6 crystals with different crystal facets, Cu_6(S), Cu_6(H), and Cu_6(P), are obtained (Figure 2). The morphologies of prepared samples of 100–3000 nm in size were characterized by scanning electron microscopy (SEM). As shown in Figure 2a,d, Cu_6(P) presents a polyhedral morphology with an exposed area ratio (~1:1.62:5.41) of the (001)/(101)/(100) facet, including the (001) facet exposing all close parallel Cu sites of the $\{Cu_3\}$ unit, the (100) facets exposing two distant Cu active sites, and the (101) facets exposing a solitary Cu site. As the $S_{(100)}$ decreases and $S_{(001)}$ increases, the hexagonal prism Cu_6(H) possesses ~200 nm thickness with the same $S_{(100)}$ and $S_{(001)}$ (Figure 2b,e). The sheet Cu_6(S) has the maximum exposed area of (001) facet surrounded by the (101) facets, which has a $S_{(001)}$:$S_{(101)}$ of about 3:1 (Figure 2c,f). The crystal facets of these samples were simulated and calculated by Mercury software. The active sites exposed on the different crystal facets are shown in Figure 2g. Overall, the variation of micro–nano crystalline morphologies from Cu_6(P) through Cu_6(H) to Cu_6(S) shows that the $S_{(100)}$ gradually decreases to disappearance, and the $S_{(001)}$ gradually increases, which indicates that the catalytic activities of the as-prepared samples are different.

The powder X-ray diffraction (PXRD) pattern proves that these as-prepared Cu_6 catalysts [Cu_6(S), Cu_6(H), and Cu_6(P)] are well-matched with their simulated

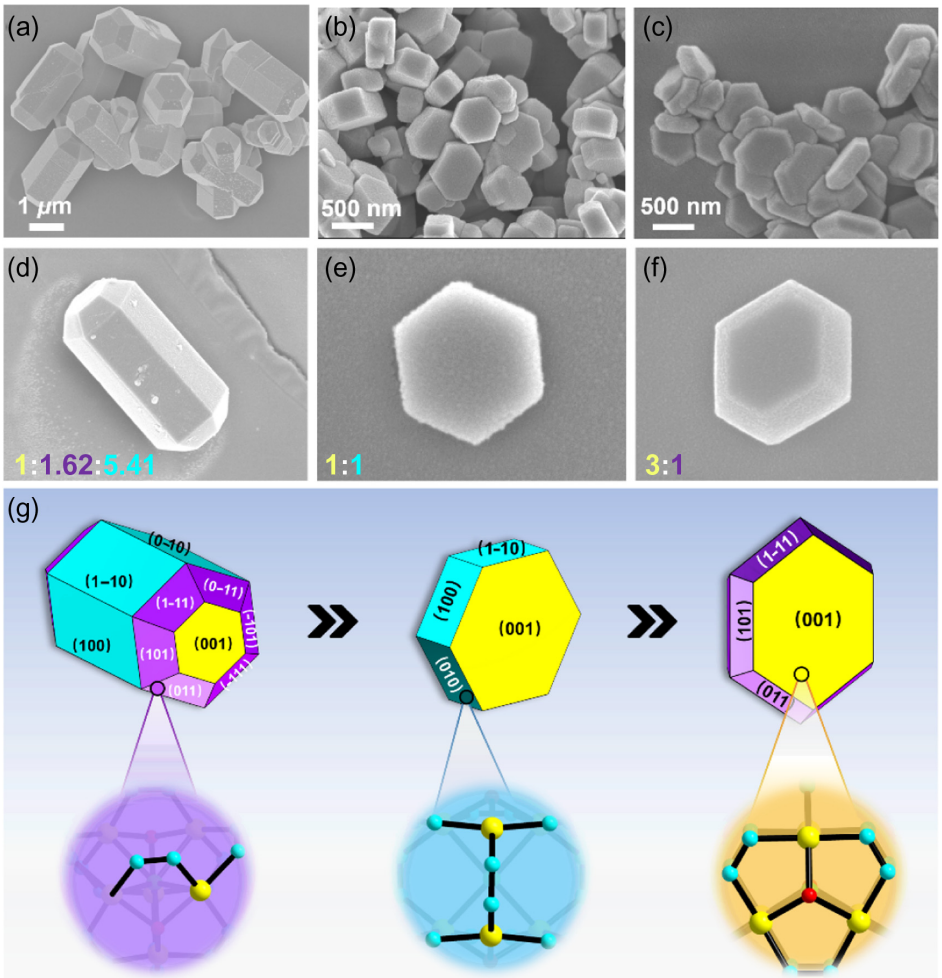

Figure 2 | *The SEM images of as-prepared Cu_6 samples. (a and d) Cu_6(P). (b and e) Cu_6(H). (c and f) Cu_6(S). (g) Schematic illustration of the evolution of morphology and the Cu active sites exposed on different facets over Cu_6(P), Cu_6(H), and Cu_6(S). All hydrogen atoms and carbon atoms are omitted for clarity.*

Citation: *CCS Chem.* **2023**, Just Published. DOI: 10.31635/ccschem.022.202202316
Link to VoR: https://doi.org/10.31635/ccschem.022.202202316

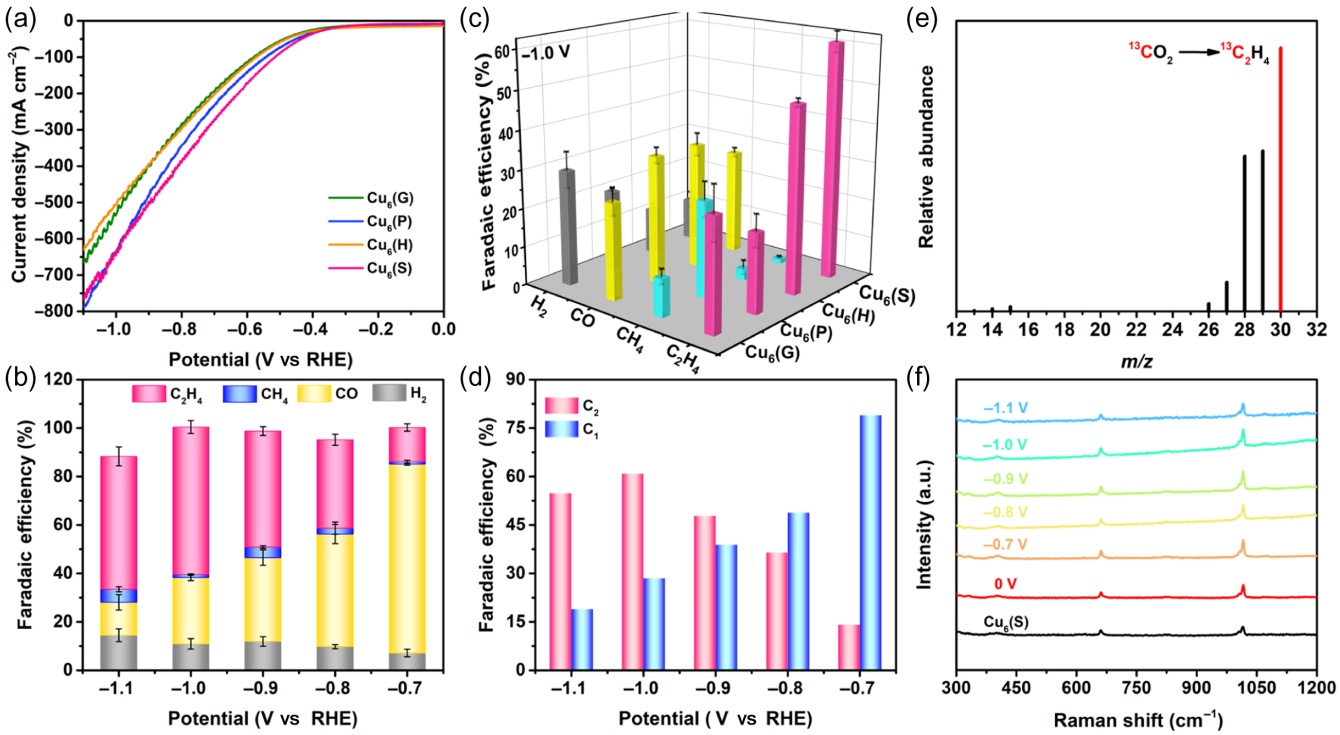

Figure 3 | *Electrocatalytic performances of as-prepared samples. (a) LSV curves in CO_2 atmosphere. (b) FE (H_2, CO, CH_4, and C_2H_4) of Cu_6(S). (c) The contrast of FE (H_2, CO, CH_4, and C_2H_4) of as-prepared samples at –1.0 V vs RHE. (d) The contrast FE of C_1 and C_2 for Cu_6(S). (e) The mass spectra from GC-MS of $^{13}C_2H_4$ product from $^{13}CO_2$ reduction for Cu_6(S). (f) In situ Raman spectra from 300 to 1200 cm^{-1} before and under CO_2RR potentials.*

patterns, suggesting the successful synthesis and high purity of these catalysts (Supporting Information Figure S5). The peaks at 7.5°, 9.7°, and 12.3° belong to (100), (101), and (001) facets, respectively (Supporting Information Figure S6). The Fourier transform infrared (FTIR) spectroscopy also confirms that the as-synthesized samples are isomorphic (Supporting Information Figure S7). Moreover, the X-ray photoelectron spectroscopy result shows that the peak at ~965 eV is attributed to Cu $2p_{1/2}$, and the peak at ~ 934 eV is attributed to Cu $2p_{3/2}$, indicating that Cu only has an oxidation state of +2 in Cu_6 (Supporting Information Figure S8). To evaluate the thermal stability of these samples, the thermogravimetric analysis was carried out under an oxygen atmosphere, and the results illustrate that they remain thermodynamically stable before heating to 275 °C (Supporting Information Figure S9). At the same time, the excellent chemical stability was evaluated by soaking these samples in 0.5 M KOH aqueous solution for 24 h at room temperature, and the PXRD and FTIR patterns imply the structures of Cu_6 catalysts remained intact in alkaline solution (Supporting Information Figures S10 and 11). To sum up the above, the high structural stability and good chemical stability of the Cu_6 catalysts are also important foundations for their further performance development.

Electrochemical CO_2 reduction performance

Given the stability of Cu_6 catalysts in alkaline solutions, 0.5 M KOH aqueous solution was chosen as the electrolyte for electrocatalytic CO_2RR testing, which can effectively inhibit the HER and reduce the activation energy barrier for C–C coupling.[38-40] All electrochemical CO_2RR tests were evaluated in a flow cell,[41,42] which can help to achieve better CO_2 utilization and higher current densities, and increase the potential for high value-added product generation. To investigate the reaction activities of these electrocatalysts, linear sweep voltammetry (LSV) polarization curves were measured at a wide potential range (0 to –1.1 V vs RHE) in atmospheres of CO_2 and Ar separately (Supporting Information Figure S12). The results demonstrate the lower onset potential and higher current density in flowing CO_2 than those in Ar atmosphere, which suggests their higher reaction activity of electrocatalytic CO_2RR than HER. It is worth noting that the current densities of Cu_6(G), Cu_6(P), Cu_6(H), and Cu_6(S) can reach 676.91, 788.59, 629.81, and 764.16 mA cm^{-2} at –1.1 V, respectively (Figure 3a).

To further evaluate the influence of the crystal-facet effects on the selectivity of different reduction products in the process of CO_2RR, the electrolysis experiments were performed at different applied potentials between –0.7 and –1.1 V (vs RHE) under a continuous flow of CO_2.

Citation: *CCS Chem.* **2023**, Just Published. DOI: 10.31635/ccschem.022.202202316
Link to VoR: https://doi.org/10.31635/ccschem.022.202202316

The detailed analysis of these catalysts in terms of CO_2RR reduction performance is as follows (Supporting Information Table S3–S6). The gaseous reduction products analyzed by on-line GC are mainly C_2H_4, CH_4, CO, and H_2 at all application potentials, and the FE_{total} of gas products is close to 100%. Furthermore, the lower concentration of liquid products detected by NMR spectroscopy cannot be accurately quantified (Supporting Information Figure S13), so we mainly focus on the selectivity differences of the gaseous products for Cu_6 catalysts during the reduction process.

At first, the blank carbon paper-modified GDL was used as an electrocatalyst to exclude the influence of the carbon paper on catalytic performance. The result in Supporting Information Figure S14 shows that the highest tested current density of carbon paper is only –32.87 mA cm^{-2} at –1.1 V and the selectivity of H_2 is almost close to the FE_{total}. Further, the spherical Cu_6(G) (~100 nm) was used as a comparative sample to investigate the effect of crystal facets averaging on the selectivity of reduction product. The test results show that the FE_{H2} remains at ~30% in the tested voltage range compared with other catalysts, along with 24.86 ± 3.60% FE_{CO}, 28.77±6.78% FE_{C2H4}, and little FE_{CH4} (~10%) at –1.0 V (vs RHE) (Supporting Information Figure S15), which implies the ground sample cannot regulate the selectivity of a specific product as we had predicted. Like most catalysts, CO is the main reduction product for these model catalysts (FE_{CO} > 30%) at lower negative potentials (<–0.8 V). As for Cu_6(P) with a maximum $S_{(100)}$, the FE_{CO} keeps decreasing from 73.22 ± 2.08% to 32.54 ± 4.03% with increasing applied potential, and the FEs of CH_4 and C_2H_4 gradually increase. At –1.0 V, the maximum FEs of CH_4 and C_2H_4 reach 24.86 ± 4.59% and 20.48 ± 4.18%, respectively (Supporting Information Figure S16).

As the $S_{(100)}$ decreases and $S_{(001)}$ increases, the FE_{CO} of Cu_6(H) decreases from 61.10 ± 2.57% to 27.75 ± 1.75% at all applied potentials, while the FE of C_2H_4 reaches the highest value of ~50% at –1.0 V with a large current density of –243.94 mA cm^{-2} (Supporting Information Figure S17). Significantly, Cu_6(S) with a maximum exposure area of the (001) facet exhibits excellent activity and selectivity for C_2H_4 in electrocatalytic CO_2RR gives the highest FE_{C2H4} (60.93 ± 2.63%) with a larger current density of –390.07 mA cm^{-2} at –1.0 V, along with 27.39 ± 1.25% FE_{CO}, 10.92 ± 2.14% FE_{H2}, and trace FE_{CH4} (Figure 3b and Supporting Information Figure S18), which are the best crystalline coordination compound catalyst values to date for the electrocatalytic reduction of CO_2 to C_2H_4 (Supporting Information Table S7). Notably, the FE_{C2H4} is nearly invariable maintaining a value above 36% over a wide potential range (–0.8 to –1.1 V) (Figure 3d). As the evolution of micro–nano crystalline morphologies of the catalysts from Cu_6(P) via Cu_6(H) to Cu_6(S), the selectivity of C_1 products (here referring to CO and CH_4) gradually decreases with $S_{(100)}$ decreasing, and the FE of C_2H_4 progressively grows with $S_{(001)}$ increasing (Figure 3c). It can be concluded that the selectivity of different reduction products is closely related to the crystal facets exposed by these catalysts.

To identify the source of carbon in the reduction products, a ^{13}C isotope labeling experiment was performed and the gas products were analyzed by GC and mass spectrometry (MS). The peaks at m/z = 17, 29, and 30 are ascribed to $^{13}CH_4$, ^{13}CO, and $^{13}C_2H_4$, respectively (Figure 3e and Supporting Information Figure S19), suggesting the carbon source of these products is indeed converted from the CO_2 reduction. Besides, to further explore the potential factors of different product selectivities, the electrochemical double-layer capacitance (C_{dl}) values were calculated from the cyclic voltammogram curves to estimate the electrochemical surface area (Supporting Information Figures S20 and S21). As expected, Cu_6(G) with a maximum C_{dl} values (10.67 mF cm^{-2}) can afford much more disordered active sites than the others. Additionally, the EIS measurement was performed to probe the electrocatalytic kinetics on the electrode/electrolyte surface at –1.0 V. As revealed by the Nyquist plots (Supporting Information Figures S22 and S23), Cu_6(P) exhibits the smallest charge transfer resistance (R_{ct}) of 4.75 Ω among the four samples, implying the fastest electron transfer from the catalyst surface to the reactant for electrocatalytic CO_2RR. However, since these catalysts belong to the same Cu_6 structure, the relevant values do not differ significantly. To explore the catalytic durability properties of these catalysts for further applications, we selected the Cu_6(S) with the highest C_2H_4 selectivity for the long-term durability test under the optimal potential of –1.0 V via chronoamperometric testing. As shown in Supporting Information Figure S18, the FE of C_2H_4 was analyzed by online GC every 30 min and remains greater than 56% with a total current density of ~700 mA cm^{-2} during the 3-h durability test.

It is worth noting that the stability of the samples after testing is also an important indicator to evaluate the excellent performance of the catalyst. To further prove the superior stability of these catalysts, a series of comparative characterizations before and after testing in the following aspects are performed. As the catalytic reaction etches the surface, these Cu_6 catalysts after testing mostly remain in their original morphology, but no obvious substances similar to the state of Cu and its oxide particles are found by the SEM (Supporting Information Figure S24). The PXRD and IR patterns of these samples before and after the electrocatalytic CO_2RR are well-matched, which illustrates that they could maintain their structural integrity after electrochemical testing (Supporting Information Figures S25 and S26). Furthermore, no peaks of Cu (0), Cu_2O, or CuO are found in the PXRD patterns of these samples, implying that Cu (+2) ions in the structure have not been converted into the above after testing.

Citation: *CCS Chem.* **2023**, Just Published. DOI: 10.31635/ccschem.022.202202316
Link to VoR: https://doi.org/10.31635/ccschem.022.202202316

Ex situ Raman spectroscopy confirmed these findings, as the Cu (0), Cu_2O, or CuO peaks were absent after testing in these samples (Supporting Information Figure S27).[30,43] To further monitor the structural stability of the catalyst under operating conditions in real-time, in situ Raman spectroscopy is performed on Cu_6(S) before and during electrocatalytic CO_2RR at different applied potentials (~−0.7 to −1.1 V) (Figure 3f). The experimental results show that the positions of the intrinsic peaks for Cu_6(S) do not change, and no new peaks are observed during the CO_2RR process. In short, the above measurements demonstrate the superior electrochemical stability of these samples and their great potential for efficient electrochemical CO_2 reduction.

Investigating structure-functional relationships

Most high-performance crystalline materials catalysts are fully grounded and sonicated for electrocatalytic reactions due to their large size, which results in the crystal facets and their active sites exposed on the catalytic surface becoming isotropic. As seen from the performance of Cu_6(G), except for the low selectivity of CH_4, the FE_S of H_2, CO, and C_2H_4 are 29.79 ± 4.68%, 24.86 ± 3.60%, and 28.77 ± 6.78% at −1.0 V, respectively. Thus, it can be inferred that the averaging of crystal facets and their exposed Cu active sites in Cu_6(G) make it difficult to effectively control the selective generation of specific reduction products.

Currently, a large amount of literature has proved that the crystal facets of a traditional Cu single crystal influence the selectivity of CO_2 reduction products, in which the (100) facet is conducive to the formation of C_2H_4.[44] However, the products corresponding to the specific crystal facets involved in this work differ from those of Cu single crystal with the same crystal facets. As Figure 4 shows, the two non-adjacent Cu sites exposed on the (100) facets can only accept the attack of two CO_2 molecules from different directions due to their long-distance (3.682 Å) and steric hindrance, which is consistent with the test results that only one CO_2 molecule can be activated by a single Cu site on the (101) facets to generate C_1 product (Figure 4a,b). From Cu_6(P) through Cu_6(H) to Cu_6 (S), the corresponding selectivity of C_1 products (here referring to CO and CH_4) gradually decreases (57.90%, 35.58%, and 28.55% at −1.0 V, respectively) as $S_{(100)}$ gradually reduces (Figure 4d). At the same time, we can see that the selectivity of the Cu_6 catalysts for C_2H_4 production increases in the order, Cu_6(P) (24.66%) < Cu_6(H) (49.45%) < Cu_6(S) (63.56%) (Figure 4c). Due to the proper spatial distance (the distance between any Cu–Cu is 3.217 Å), the three close adjacent Cu sites located on the (001) facet can accept the attack of multiple CO_2 molecules from the same direction, which is very suitable for C–C coupling to generate C_2 products. In this regard, Cu_3-Br in our previous work exhibits excellent C_2H_4 selectivity in electrocatalytic CO_2RR, which also provides favorable evidence validating the above conclusions.[30] Therefore, owing to the various spatial distribution of catalytic active sites on different crystal facets, it can be concluded that the crystal-facet effect of the crystalline coordination compound does affect the electrocatalytic product species and reaction paths.

As with Cu-based nanomaterials, the number, spatial arrangement (position, distance, and angle), and the exposed coordination space for the orientation of CO_2 adsorption of Cu active sites exposed on different crystal facets in crystalline materials are crucial to the activity and selectivity of electrocatalytic CO_2 reduction products. From the spatial arrangement of the crystalline coordination compound, the macroscopic morphology of the Cu_6 cluster is formed by the periodic close packing of countless unit cells, so a unit cell can be regarded as a whole.[45] As shown in Supporting Information Figure S28, the unit cell contains two spatially symmetric Cu_6 molecules, and the active sites exposed on different crystal facets in the unit cell are the same as those exposed by the individual Cu_6 clusters, with the active sites exposed by the (101), (100), and (001) facets being 1, 2, and 3, respectively. Immediately afterward, the areas of the unit cell toward the different crystal facets are calculated separately, and detailed calculation information is provided in Table 1. In this case, the number of unit cells of different crystal facets ($N_{(hkl)}$) can be calculated according to the real morphology provided by SEM, which is key to analyzing the selective catalysis of three kinds of morphologies catalysts with different facets on C_1/C_2 reduction products (Supporting Information Table S8). Cu_6(P) combines all the crystal facets of Cu_6(S) and Cu_6(H), which estimates the ratio of area exposed on (001)/(101)/(100) facets to be ~1:1.62:5.41, with the corresponding $N_{(001)}$:$N_{(101)}$:$N_{(100)}$ ≈ 1:2.20:4.42. And for Cu_6(H), the $S_{(001)}$:$S_{(100)}$ and the $N_{(001)}$:$N_{(100)}$ are both ~1:1. The Cu_6(S) exposed (001)/(101) facets area ratio is about 3:1, leading to the value of $N_{(001)}$:$N_{(101)}$ being 2:1. It can be seen that the ratio of $S_{(hkl)}$ and $N_{(hkl)}$ for the Cu_6 catalysts follows the same trend, which is also in agreement with experimental results. The more exposed area of (001) facet, the more active sites for C_2H_4 production.

In situ characterization

To detect reaction intermediates during the CO_2RR process, the in-situ diffuse reflaxions infrared Fourier transformations spectroscopy (DRIFTS) measurements were performed. As shown in Figure 5a, the downward band at 2331 and 2362 cm^{-1} is associated with CO_2.[46] The intensity of the peak decreases with increasing electrolysis time, showing that the CO_2 is gradually consumed. The absorption peaks at 1336 and 1396 cm^{-1} can be attributed to

Citation: *CCS Chem.* **2023**, Just Published. DOI: 10.31635/ccschem.022.202202316
Link to VoR: https://doi.org/10.31635/ccschem.022.202202316

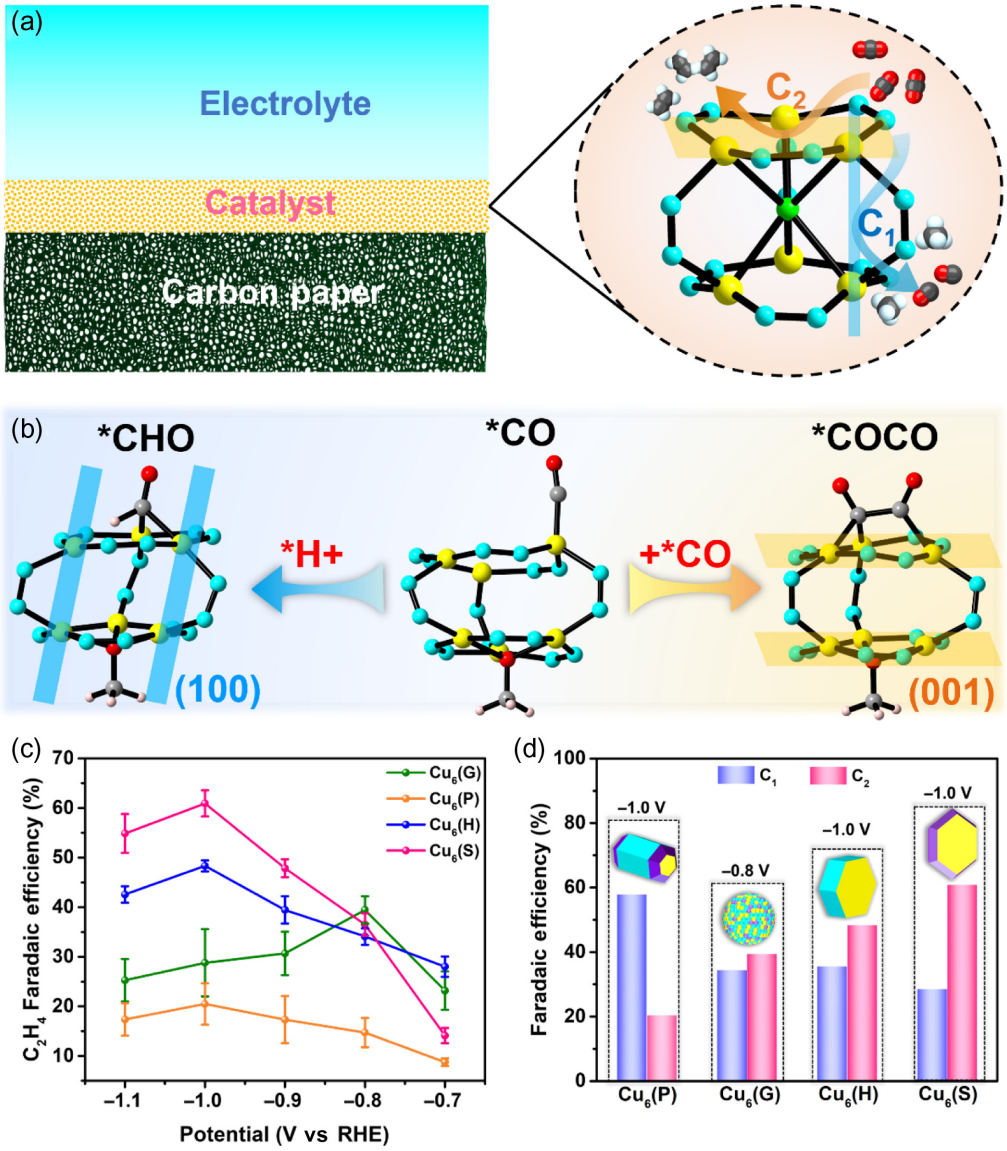

Figure 4 | *Exploring the potential relationship between crystal-facet effect and performance. (a) Schematic diagram of the catalytic selectivity of different crystal facets in GDL. (b) The important intermediate for generating C_1 or C_2 on the different facets. (c) The contrast of partial current density of C_2H_4 for as-prepared samples at all test potentials. (d) Comparison of the maximum FE_{C2} and corresponding FE_{C1} of Cu_6 catalysts.*

the C–O stretching and symmetric stretching of the *COOH intermediate, separately,[47] and the very weak signal of the *CO intermediate is detected at 2063 cm^{-1}, which is close to the position of the *CO intermediate (ca. 2058 cm^{-1}) reported in the literature under an alkaline environment.[48] Additionally, we also detect the peak at 1025 cm^{-1} corresponding to the nonplanar vibration (O=C–H) of the *CHO intermediate.[46,49] The absorption peaks at 881 and 3120 cm^{-1} could be assigned to the C–H bending vibration and stretching of the *CH_2= intermediate, respectively. Most importantly, the CO dimer (*CO-CO) presents a vibrational band at 1200 cm^{-1}, and then the absorption peaks at 1214 and 1560 cm^{-1} could be attributed to the hydrogenated *COCO intermediate (*OCCHO); both of which are commonly recognized as essential intermediates in the electrocatalytic CO_2 reduction to C_2H_4.[48,50]

DFT calculations

DFT calculations were carried out to investigate the specific reaction paths and more detailed intermediates in this process. Based on the accurate crystal structure model, the adsorption energy of the μ-OCH_3 binding with an H^+/e^- was discovered to be relatively low during the calculation process, which is beneficial for the adsorption and activation of CO_2 substrate molecules (Supporting Information Figure S28). The two non-adjacent Cu sites

Citation: *CCS Chem.* **2023**, Just Published. DOI: 10.31635/ccschem.022.202202316
Link to VoR: https://doi.org/10.31635/ccschem.022.202202316

Table 1 | *Area Calculations of Single Unit Cells of Different Crystal Facets*

Crystal Facet	Single Unit Cell Diagram of Crystal Facet	Area Calculation of Single Unit Cell of Crystal Facet
(101)	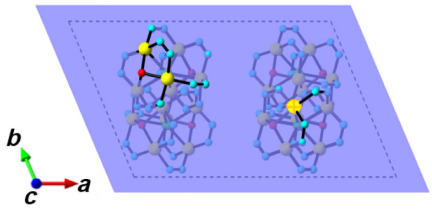	Lattice parameters:[a] *a* 19.82 Å α 110° *b* 13.55 Å β 93.70° *c* 19.82 Å γ 110° $S_{(101)}$ = 1.18 nm^2
(100)	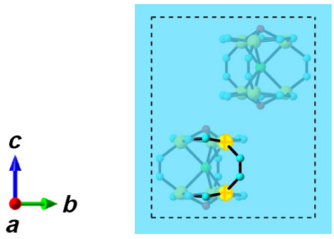	Lattice parameters: *a* 13.55 Å α 90° *b* 13.55 Å β 90° *c* 14.45 Å γ 120° $S_{(100)}$ = 1.96 nm^2
(001)	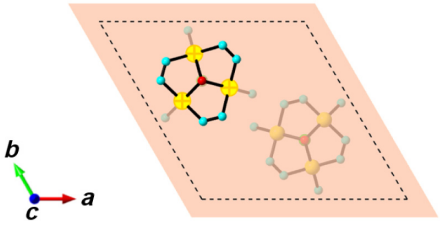	Lattice parameters: *a* 13.55 Å α 90° *b* 13.55 Å β 90° *c* 14.45 Å γ 120° $S_{(001)}$ = 1.60 nm^2

[a] Lattice parameters of (101): to calculate the unit cell area of the (101) facets, the unit cell model with the *c*-axis trending as (101) facet is reconstructed; the active sites exposed on the different crystal facets in the diagram have been marked with crosses.

on the (100) facets were located far apart (3.682 Å) and steric hindrance cannot carry out effective C–C coupling, because the two adsorbed *CO intermediates are oriented in opposite directions. The only single Cu active site of the (101) facets can only adsorb one *CO intermediate. Consequently, the Cu active sites exposed on the two kinds of crystal facets are suitable for the generation of C_1 products. From the experimental results, the amount of CO production decreases with the formation of CH_4 and C_2H_4, so it can be inferred that the *CO intermediate (* indicates the adsorption site) exists in the conversion pathway from CO_2 to CH_4/C_2H_4.[28] As shown in Figure 5b and Supporting Information Table S9, it provides the specific reaction path and the corresponding optimized structure of all intermediates generated for the reduction of CO_2 to C_1 on the Cu active site. The Gibbs free energy diagram also shows a negative free energy change throughout the process, suggesting the reduction process is thermodynamically favorable. The gas-phase CO_2 molecules are first adsorbed on a single catalytic Cu site and rapidly converted to *COOH by hydrogenation, which is considered to be the rate-determining step (RDS) for CO generation. Subsequently, the *CO intermediate obtained by hydrogenation and dehydration of *COOH is successively reduced to*CHO, *CHOH, *CH_2OH, *CH_2, and *CH_3 through multi-step proton-electron transfer processes, and finally, the reduction product CH_4 (g) is obtained.[51] Particularly, the step of converting *CHO to *CHOH is critical for CH_4 generation. Then we explore the possible ways of C–C coupling on the Cu active sites of (001) facet. The C–C coupling is initiated from the *CO intermediate (* indicates the adsorption site). The dynamic calculation result shows that the energy of the transition state from *CO to *COCO is lower than that to *CO–CHO (Supporting Information Figure S29), suggesting that the three adjacent Cu active sites on the (001) facet help to stabilize the key intermediates of *COCO due to their close distance and suitable spatial distance. As displayed in Supporting Information Table S10, the main intermediates and energies involved in each pathway from CO_2 to C_2H_4 are summarized and compared in detail, and the corresponding optimized structures of all intermediates in the reaction pathway with the lowest energy are provided. The final reduction path, *COCO → *CO-CHO → *CHO-CHO → *CHO-CH_2O → *CHOH-CH_2O → *CH_2OH-CH_2O → *CH_2-CH_2O → C_2H_4(g) with corresponding free energy changes of –0.261, –0.514, –0.644,

Citation: *CCS Chem.* **2023**, Just Published. DOI: 10.31635/ccschem.022.202202316
Link to VoR: https://doi.org/10.31635/ccschem.022.202202316

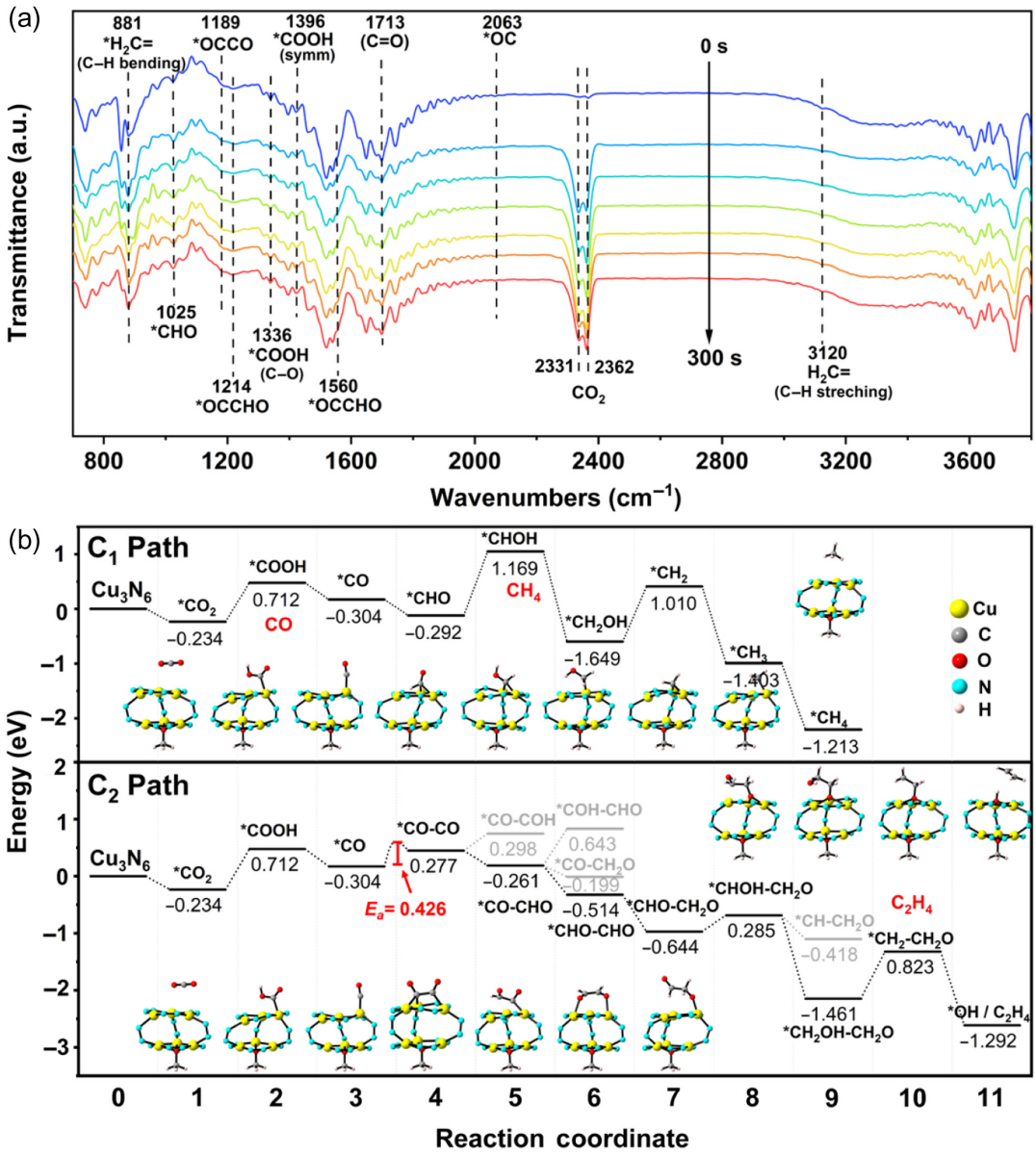

Figure 5 | *In situ DRIFTS and DFT calculations. (a) The in situ DRIFTS spectra of Cu_6(S). (b) Free energy diagrams and optimized structure of C_1 and C_2 pathways and all possible paths energy comparison of CO_2RR reduction to C_2H_4 on Cu_6 catalysts.*

0.285, –1.461, and 0.823 eV, is the optimal reaction path.[52] It is noteworthy that the step of $^*CH_2OH\text{-}CH_2O \rightarrow {}^*CH_2\text{-}CH_2O$ exhibiting the largest free energy (0.823 eV) is the RDS. In conclusion, the DFT calculations further confirm our prediction of the difference in catalytic selectivity of C_1 or C_2 reduction products on various crystal facets, which is consistent with the final experimental results.

Conclusions

In summary, we designed and synthesized a well-defined crystalline coordination compound model (Cu_6), where Cu active sites located in various crystal facets have different numbers, spatial arrangements, and exposed coordination spaces for the orientation of CO_2 adsorption. With the aid of surfactants, the micro–nano crystalline morphologies of the Cu_6 catalysts [Cu_6(P), Cu_6(H), and Cu_6(S)] were effectively regulated. From Cu_6(P) through Cu_6(H) to Cu_6(S), the corresponding selectivity of CO_2 reduction to C_1 products (CO and CH_4) gradually decreases with C_2 (C_2H_4) increasing. This is the first work able to effectively control the morphology of crystalline coordination cluster catalysts to the micro–nano size, and systematically study the important effects of crystal facet effects on the selective generation of C_1 or C_2 reduction products.

Citation: *CCS Chem.* **2023**, Just Published. DOI: 10.31635/ccschem.022.202202316
Link to VoR: https://doi.org/10.31635/ccschem.022.202202316

Supporting Information

Supporting Information is available and includes the details of experimental instruments and measurement processes, the synthesis and characterization of these samples, active sites exposed to different crystal facets in Cu_6 structure, electrocatalytic test results of Cu_6 catalysts, the ^{1}H NMR characterization of the liquid product, and DFT calculations results.

Conflict of Interest

There is no conflict of interest to report.

Funding Information

This study was financially supported by the NSFC (grant nos. 92061101, 21871141, and 22225109), the Excellent Youth Foundation of Jiangsu Natural Science Foundation (grant no. BK20211593), Postgraduate Research & Practice Innovation Program of Jiangsu Province (KYCX22_1546), Priority Academic Program Development of Jiangsu Higher Education Institutions, and the Foundation of Jiangsu Collaborative Innovation Center of Biomedical Functional Materials.

References

1. Ding, M.; Flaig, R. W.; Jiang, H. L.; Yaghi, O. M. Carbon Capture and Conversion Using Metal-Organic Frameworks and MOF-Based Materials. *Chem. Soc. Rev.* **2019**, *48*, 2783–2828.
2. Jia, S.; Ma, X.; Sun, X.; Han, B. Electrochemical Transformation of CO_2 to Value-Added Chemicals and Fuels. *CCS Chem.* **2022**, *4*, 3213–3229.
3. Gao, D.; Arán-Ais, R. M.; Jeon, H. S.; Roldan Cuenya, B. Rational Catalyst and Electrolyte Design for CO_2 Electroreduction Towards Multicarbon Products. *Nat. Catal.* **2019**, *2*, 198–210.
4. Vasileff, A.; Xu, C. C.; Jiao, Y.; Zheng, Y.; Qiao, S. Z. Surface and Interface Engineering in Copper-Based Bimetallic Materials for Selective CO_2 Electroreduction. *Chem.* **2018**, *4*, 1809–1831.
5. Rong, W.; Zou, H.; Tan, S.; Hu, E.; Li, F.; Tang, C.; Dai, H.; Wei, S.; Ji, Y.; Duan, L. Few-Atom Copper Catalyst for the Electrochemical Reduction of CO to Acetate: Synergetic Catalysis between Neighboring Cu Atoms. *CCS Chem.* **2022**. DOI: https://doi.org/10.31635/ccschem.022.202201910
6. Reske, R.; Mistry, H.; Behafarid, F.; Roldan Cuenya, B.; Strasser, P. Particle Size Effects in the Catalytic Electroreduction of CO_2 on Cu Nanoparticles. *J. Am. Chem. Soc.* **2014**, *136*, 6978–6986.
7. Rong, W. F.; Zou, H. Y.; Zang, W. J.; Xi, S. B.; Wei, S. T.; Long, B. H.; Hu, J. H.; Ji, Y. F.; Duan, L. L. Size-Dependent Activity and Selectivity of Atomic-Level Cu Nanoclusters During CO/CO_2 Electroreduction. *Angew. Chem. Int. Ed.* **2020**, *60*, 466–472.
8. Deng, B. W.; Huang, M.; Li, K. L.; Zhao, X. L.; Geng, Q.; Chen, S.; Xie, H. T.; Dong, X. a.; Wang, H.; Dong, F. Crystal Plane Is Not the Key Factor for CO_2-to-Methane Electrosynthesis on Reconstructed Cu_2O Microparticles. *Angew. Chem. Int. Ed.* **2021**, *61*, 202114080.
9. Chen, Y.; Fan, Z. X.; Wang, J.; Ling, C. Y.; Niu, W. X.; Huang, Z. Q.; Liu, G. G.; Chen, B.; Lai, Z. C.; Liu, X. Z.; Li, B.; Zong, Y.; Gu, L.; Wang, J. L.; Wang, X.; Zhang, H. Ethylene Selectivity in Electrocatalytic CO_2 Reduction on Cu Nanomaterials: A Crystal Phase-Dependent Study. *J. Am. Chem. Soc.* **2020**, *142*, 12760–12766.
10. Zhong, D. Z.; Zhao, Z. J.; Zhao, Q.; Cheng, D. F.; Liu, B.; Zhang, G.; Deng, W. Y.; Dong, H.; Zhang, L.; Li, J. K.; Li, J. P.; Gong, J. L. Coupling of Cu(100) and (110) Facets Promotes Carbon Dioxide Conversion to Hydrocarbons and Alcohols. *Angew. Chem. Int. Ed.* **2020**, *60*, 4879–4885.
11. Li, H.; Yu, P. P.; Lei, R. B.; Yang, F. P.; Wen, P.; Ma, X.; Zeng, G. S.; Guo, J. H.; Toma, F. M.; Qiu, Y. J.; Geyer, S. M.; Wang, X. W.; Cheng, T.; Drisdell, W. S. Facet-Selective Deposition of Ultrathin Al_2O_3 on Copper Nanocrystals for Highly Stable CO_2 Electroreduction to Ethylene. *Angew. Chem. Int. Ed.* **2021**, *60*, 24838–24843.
12. Choi, C.; Kwon, S.; Cheng, T.; Xu, M.; Tieu, P.; Lee, C.; Cai, J.; Lee, H. M.; Pan, X. Q.; Duan, X. F.; Goddard, W. A.; Huang, Y. Highly Active and Stable Stepped Cu Surface for Enhanced Electrochemical CO_2 Reduction to C_2H_4. *Nat. Catal.* **2020**, *3*, 804–812.
13. Roberts, F. S.; Kuhl, K. P.; Nilsson, A. High Selectivity for Ethylene from Carbon Dioxide Reduction over Copper Nanocube Electrocatalysts. *Angew. Chem. Int. Ed.* **2015**, *54*, 5179–5182.
14. Zhang, X.; Sa, R.; Zhou, F.; Rui, Y.; Liu, R.; Wen, Z.; Wang, R. Metal-Organic Framework-Derived CuS Nanocages for Selective CO_2 Electroreduction to Formate. *CCS Chem.* **2021**, *3*, 199–207.
15. Lee, S. H.; Lin, J. C.; Farmand, M.; Landers, A. T.; Feaster, J. T.; Avilés Acosta, J. E.; Beeman, J. W.; Ye, Y.; Yano, J.; Mehta, A.; Davis, R. C.; Jaramillo, T. F.; Hahn, C.; Drisdell, W. S. Oxidation State and Surface Reconstruction of Cu Under CO_2 Reduction Conditions from in Situ X-Ray Characterization. *J. Am. Chem. Soc.* **2021**, *143*, 588–592.
16. Yang, P. P.; Zhang, X. L.; Gao, F. Y.; Zheng, Y. R.; Niu, Z. Z.; Yu, X. X.; Liu, R.; Wu, Z. Z.; Qin, S.; Chi, L. P.; Duan, Y.; Ma, T.; Zheng, X. S.; Zhu, J. F.; Wang, H. J.; Gao, M. R.; Yu, S. H. Protecting Copper Oxidation State via Intermediate Confinement for Selective CO_2 Electroreduction to C_{2+} Fuels. *J. Am. Chem. Soc.* **2020**, *142*, 6400–6408.
17. Liu, H.; Yang, B. Potential-Dependent C–C Coupling Mechanism and Activity of C_2 Formation in the Electrocatalytic Reduction of CO_2 on Defective Cu(100) Surfaces. *Chem. Commun.* **2022**, *58*, 709–712.
18. Mistry, H.; Varela, A. S.; Bonifacio, C. S.; Zegkinoglou, I.; Sinev, I.; Choi, Y. W.; Kisslinger, K.; Stach, E. A.; Yang, J. C.; Strasser, P.; Cuenya, B. R. Highly Selective Plasma-Activated Copper Catalysts for Carbon Dioxide Reduction to Ethylene. *Nat. Commun.* **2016**, *7*, 12123.

Citation: *CCS Chem.* **2023**, Just Published. DOI: 10.31635/ccschem.022.202202316
Link to VoR: https://doi.org/10.31635/ccschem.022.202202316

19. Ren, F.; Hu, W.; Wang, C.; Wang, P.; Li, W.; Wu, C.; Yao, Y.; Luo, W.; Zou, Z. An Extrinsic Faradaic Layer on CuSn for High-Performance Electrocatalytic CO_2 Reduction. *CCS Chem.* **2022**, *4*, 1610–1618.
20. Zhou, Y. S.; Che, F. L.; Liu, M.; Zou, C. Q.; Liang, Z. Q.; De Luna, P.; Yuan, H. F.; Li, J.; Wang, Z. Q.; Xie, H. P.; Li, H. M.; Chen, P. N.; Bladt, E.; Quintero-Bermudez, R.; Sham, T. K.; Bals, S.; Hofkens, J.; Sinton, D.; Chen, G.; Sargent, E. H. Dopant-Induced Electron Localization Drives CO_2 Reduction to C_2 Hydrocarbons. *Nat. Chem.* **2018**, *10*, 974–980.
21. Yu, S.; Louisia, S.; Yang, P. D. The Interactive Dynamics of Nanocatalyst Structure and Microenvironment During Electrochemical CO_2 Conversion. *JACS Au.* **2022**, *2*, 562–572.
22. Xiao, X.; Zou, L. L.; Pang, H.; Xu, Q. Synthesis of Micro/Nanoscaled Metal-Organic Frameworks and Their Direct Electrochemical Applications. *Chem. Soc. Rev.* **2020**, *49*, 301–331.
23. Lu, S.; Liang, J.; Long, H.; Li, H.; Zhou, X.; He, Z.; Chen, Y.; Sun, H.; Fan, Z.; Zhang, H. Crystal Phase Control of Gold Nanomaterials by Wet-Chemical Synthesis. *Acc. Chem. Res.* **2020**, *53*, 2106–2118.
24. Ren, W.; Zhao, C. Paths Towards Enhanced Electrochemical CO_2 Reduction. *Natl. Sci. Rev.* **2020**, *7*, 7–9.
25. Hou, Y.; Huang, Y.-B.; Liang, Y.-L.; Chai, G.-L.; Yi, J.-D.; Zhang, T.; Zang, K.-T.; Luo, J.; Xu, R.; Lin, H.; Zhang, S.-Y.; Wang, H.-M.; Cao, R. Unraveling the Reactivity and Selectivity of Atomically Isolated Metal-Nitrogen Sites Anchored on Porphyrinic Triazine Frameworks for Electroreduction of CO_2. *CCS Chem.* **2019**, *1*, 384–395.
26. Sun, S.-N.; Li, N.; Liu, J.; Ji, W.-X.; Dong, L.-Z.; Wang, Y.-R.; Lan, Y.-Q. Identification of the Activity Source of CO_2 Electroreduction by Strategic Catalytic Site Distribution in Stable Supramolecular Structure System. *Natl. Sci. Rev.* **2021**, *8*, nwaa195.
27. Wang, Y. R.; Yang, R. X.; Chen, Y. F.; Gao, G. K.; Wang, Y. J.; Li, S. L.; Lan, Y. Q. Chloroplast-like Porous Bismuth-Based Core–Shell Structure for High Energy Efficiency CO_2 Electroreduction. *Sci. Bull.* **2020**, *65*, 1635–1642.
28. Zhang, Y.; Dong, L. Z.; Li, S.; Huang, X.; Chang, J. N.; Wang, J. H.; Zhou, J.; Li, S. L.; Lan, Y. Q. Coordination Environment Dependent Selectivity of Single-Site-Cu Enriched Crystalline Porous Catalysts in CO_2 Reduction to CH_4. *Nat. Commun.* **2021**, *12*, 6390.
29. Zhang, L.; Li, X. X.; Lang, Z. L.; Liu, Y.; Liu, J.; Yuan, L.; Lu, W. Y.; Xia, Y. S.; Dong, L. Z.; Yuan, D. Q.; Lan, Y. Q. Enhanced Cuprophilic Interactions in Crystalline Catalysts Facilitate the Highly Selective Electroreduction of CO_2 to CH_4. *J. Am. Chem. Soc.* **2021**, *143*, 3808–3816.
30. Lu, Y. F.; Dong, L. Z.; Liu, J.; Yang, R. X.; Liu, J. J.; Zhang, Y.; Zhang, L.; Wang, Y. R.; Li, S. L.; Lan, Y. Q. Predesign of Catalytically Active Sites via Stable Coordination Cluster Model System for Electroreduction of CO_2 to Ethylene. *Angew. Chem. Int. Ed.* **2021**, *60*, 26210–26217.
31. Wang, R.; Liu, J.; Huang, Q.; Dong, L. Z.; Li, S. L.; Lan, Y. Q. Partial Coordination-Perturbed Bi-Copper Sites for Selective Electroreduction of CO_2 to Hydrocarbons. *Angew. Chem. Int. Ed.* **2021**, *60*, 19829–19835.
32. Jeong, H. M.; Kwon, Y.; Won, J. H.; Lum, Y. w.; Cheng, M. J.; Kim, K. H.; Head Gordon, M.; Kang, J. K. Atomic-Scale Spacing Between Copper Facets for the Electrochemical Reduction of Carbon Dioxide. *Adv. Energy Mater.* **2020**, *10*, 1903423.
33. Peng, J.; Chen, B. L.; Wang, Z. C.; Guo, J.; Wu, B. H.; Hao, S. Q.; Zhang, Q. H.; Gu, L.; Zhou, Q.; Liu, Z.; Hong, S. Q.; You, S. F.; Fu, A.; Shi, Z. F.; Xie, H.; Cao, D. Y.; Lin, C. J.; Fu, G.; Zheng, L. S.; Jiang, Y.; Zheng, N. F. Surface Coordination Layer Passivates Oxidation of Copper. *Nature.* **2020**, *586*, 390–394.
34. Wang, Y. R.; Huang, Q.; He, C. T.; Chen, Y. F.; Liu, J.; Shen, F. C.; Lan, Y. Q. Oriented Electron Transmission in Polyoxometalate-Metalloporphyrin Organic Framework for Highly Selective Electroreduction of CO_2. *Nat. Commun.* **2018**, *9*, 4466.
35. Liu, Y.; Zhao, G.; Wang, D.; Li, Y. Heterogeneous Catalysis for Green Chemistry Based on Nanocrystals. *Natl. Sci. Rev.* **2015**, *2*, 150–166.
36. Zaza, L.; Rossi, K.; Buonsanti, R. Well-Defined Copper-Based Nanocatalysts for Selective Electrochemical Reduction of CO_2 to C_2 Products. *ACS Energy Lett.* **2022**, 1284–1291.
37. Zhou, W.; Li, W.; Wang, J. Q.; Qu, Y.; Yang, Y.; Xie, Y.; Zhang, K. F.; Wang, L.; Fu, H. G.; Zhao, D. Y. Ordered Mesoporous Black TiO_2 as Highly Efficient Hydrogen Evolution Photocatalyst. *J. Am. Chem. Soc.* **2014**, *136*, 9280–9283.
38. Lv, J. J.; Jouny, M.; Luc, W.; Zhu, W. L.; Zhu, J. J.; Jiao, F. A Highly Porous Copper Electrocatalyst for Carbon Dioxide Reduction. *Adv. Mater.* **2018**, *30*, 1803111.
39. Nitopi, S.; Bertheussen, E.; Scott, S. B.; Liu, X.; Engstfeld, A. K.; Horch, S.; Seger, B.; Stephens, I. E. L.; Chan, K.; Hahn, C.; Nørskov, J. K.; Jaramillo, T. F.; Chorkendorff, I. Progress and Perspectives of Electrochemical CO_2 Reduction on Copper in Aqueous Electrolyte. *Chem. Rev.* **2019**, *119*, 7610–7672.
40. Zhang, Z.; Melo, L.; Jansonius, R. P.; Habibzadeh, F.; Grant, E. R.; Berlinguette, C. P. pH Matters When Reducing CO_2 in an Electrochemical Flow Cell. *ACS Energy Lett.* **2020**, *5*, 3101–3107.
41. Burdyny, T.; Smith, W. A. CO_2 Reduction on Gas-Diffusion Electrodes and Why Catalytic Performance Must Be Assessed at Commercially-Relevant Conditions. *Energy Environ. Sci.* **2019**, *12*, 1442–1453.
42. Kuhl, K. P.; Cave, E. R.; Abram, D. N.; Jaramillo, T. F. New Insights into the Electrochemical Reduction of Carbon Dioxide on Metallic Copper Surfaces. *Energy Environ. Sci.* **2012**, *5*, 7050–7059.
43. Niveditha, C. V.; Fatima, M. J. J.; Sindhu, S. Comprehensive Interfacial Study of Potentio-Dynamically Synthesized Copper Oxide Thin Films for Photoelectrochemical Applications. *J. Electrochem. Soc.* **2016**, *163*, H426–H433.
44. Hori, Y.; Takahashi, I.; Koga, O.; Hoshi, N. Electrochemical Reduction of Carbon Dioxide at Various Series of Copper Single Crystal Electrodes. *J. Mol. Catal. A Chem.* **2003**, *199*, 39–47.
45. Xiong, W.; Gu, X. K.; Zhang, Z.; Chai, P.; Zang, Y.; Yu, Z.; Li, D.; Zhang, H.; Liu, Z.; Huang, W. Fine Cubic Cu_2O Nanocrystals as Highly Selective Catalyst for Propylene Epoxidation with Molecular Oxygen. *Nat. Commun.* **2021**, *12*, 5921.

Citation: *CCS Chem.* **2023**, Just Published. DOI: 10.31635/ccschem.022.202202316
Link to VoR: https://doi.org/10.31635/ccschem.022.202202316

46. Yi, J. D.; Xie, R. K.; Xie, Z. L.; Chai, G. L.; Liu, T. F.; Chen, R. P.; Huang, Y. B.; Cao, R. Highly Selective CO_2 Electroreduction to CH_4 by in Situ Generated Cu_2O Single-Type Sites on a Conductive MOF: Stabilizing Key Intermediates with Hydrogen Bonding. *Angew. Chem. Int. Ed.* **2020**, *59*, 23641–23648.
47. Liu, Y. M.; Chen, S.; Quan, X.; Yu, H. T. Efficient Electrochemical Reduction of Carbon Dioxide to Acetate on Nitrogen-Doped Nanodiamond. *J. Am. Chem. Soc.* **2015**, *137*, 11631–11636.
48. Pérez-Gallent, E.; Figueiredo, M. C.; Calle-Vallejo, F.; Koper, M. T. M. Spectroscopic Observation of a Hydrogenated CO Dimer Intermediate During CO Reduction on Cu(100) Electrodes. *Angew. Chem. Int. Ed.* **2017**, *56*, 3621–3624.
49. Ewing, G. E.; Thompson, W. E.; Pimentel, G. C. Infrared Detection of the Formyl Radical HCO. *J. Chem. Phys.* **1960**, *32*, 927–932.
50. Qiu, X. F.; Zhu, H. L.; Huang, J. R.; Liao, P. Q.; Chen, X. M. Highly Selective CO_2 Electroreduction to C_2H_4 Using a Metal–Organic Framework with Dual Active Sites. *J. Am. Chem. Soc.* **2021**, *143*, 7242–7246.
51. Luo, W.; Nie, X.; Janik, M. J.; Asthagiri, A. Facet Dependence of CO_2 Reduction Paths on Cu Electrodes. *ACS Catal.* **2015**, *6*, 219–229.
52. Mangione, G.; Huang, J.; Buonsanti, R.; Corminboeuf, C. Dual-Facet Mechanism in Copper Nanocubes for Electrochemical CO_2 Reduction into Ethylene. *J. Phys. Chem. Lett.* **2019**, *10*, 4259–4265.

Citation: *CCS Chem.* **2023**, Just Published. DOI: 10.31635/ccschem.022.202202316
Link to VoR: https://doi.org/10.31635/ccschem.022.202202316